Supplementary Material: Following the non-thermal phase transition in niobium dioxide by time-resolved harmonic spectroscopy

Z. Nie[1],* L. Guery[1], E. B. Molinero[2], P. Juergens[1,3], T. J. van den Hooven[1], Y. Wang[4], A. Jimenez Galan[3], P. C. M. Planken[1,5], R. E. F. Silva[2,3], and P. M. Kraus[1,6†]

[1]*Advanced Research Center for Nanolithography, Science Park 106, 1098 XG Amsterdam, The Netherlands.*

[2]*Instituto de Ciencia de Materiales de Madrid, Consejo Superior de Investigaciones Científicas (ICMM-CSIC), E-28049 Madrid, Spain.*

[3]*Max-Born-Institute for Nonlinear Optics and Short Pulse Spectroscopy, Max-Born-Strasse 2A, D-12489 Berlin, Germany.*

[4]*School of physics and electronic engineering, Taishan University, 25 Dongyue Street271000 Tai'an Shandong, China.*

[5]*Van der Waals-Zeeman Institute, University of Amsterdam, Science Park 904, 1098 XH Amsterdam, The Netherlands.*

[6]*Department of Physics and Astronomy, and LaserLaB, Vrije Universiteit, De Boelelaan 1105,1081 HV Amsterdam, The Netherlands.*

(Dated: November 3, 2023)

I. SUPPLEMENTARY FIGURES

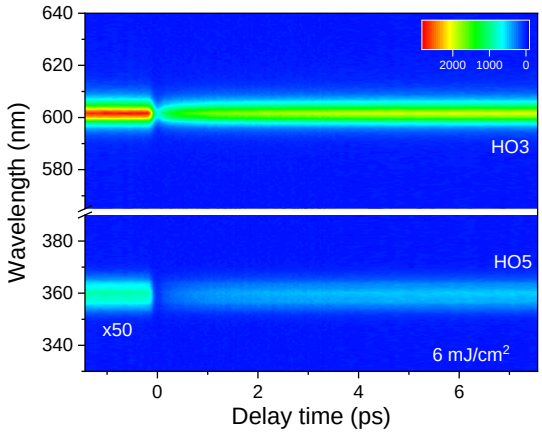

Fig. S1. 2D map of transient HHG spectroscopy, including HO3 and HO5, excited by a fluence of 6 mJ/cm^2. A short-pass filter was used to reduce the signal intensity of HO3.

* z.nie@arcnl.nl

† p.kraus@arcnl.nl

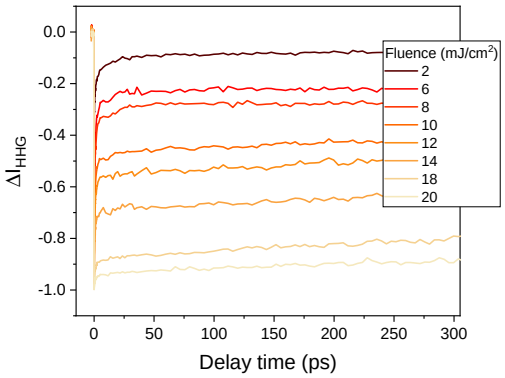

Fig. S2 Transient change of HO3 within a long delay time, suggesting that HHG suppression could persist hundreds of ps

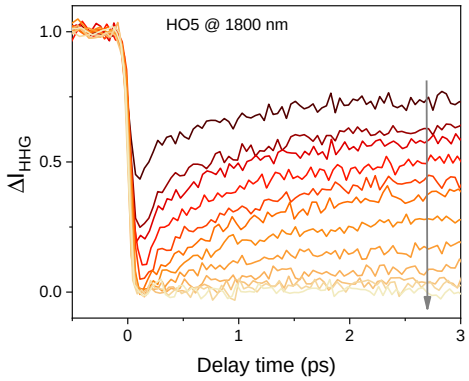

Fig. S3 Dynamical curves of HO5 suppression under several excitation fluences.

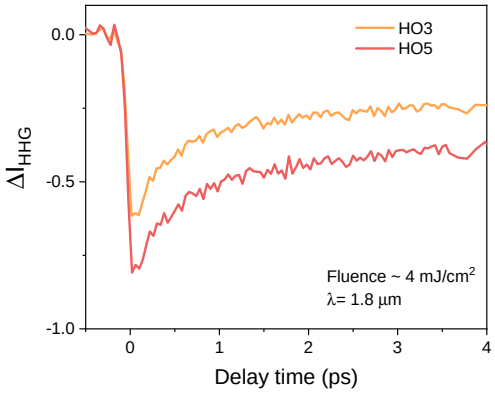

Fig. S4 The dynamical comparison between HO3 and HO5, and higher order signals display a larger response at the same conditions.

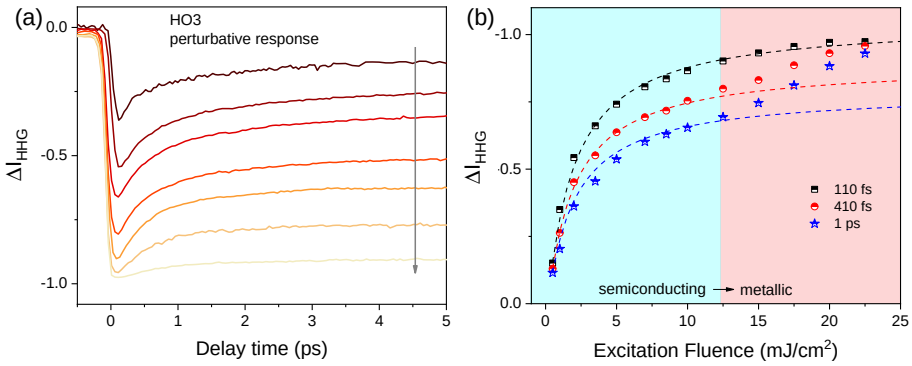

Fig. S5 Transient HO3 at the perturbative regime. (a) Dynamical curves of HO3 at different excitation fluences, showing a similar change. (b) Transient change of HO3 as a function of the excitation fluence. The dashed lines are from the saturation model, and a similar model deviation can be observed at a similar fluence.

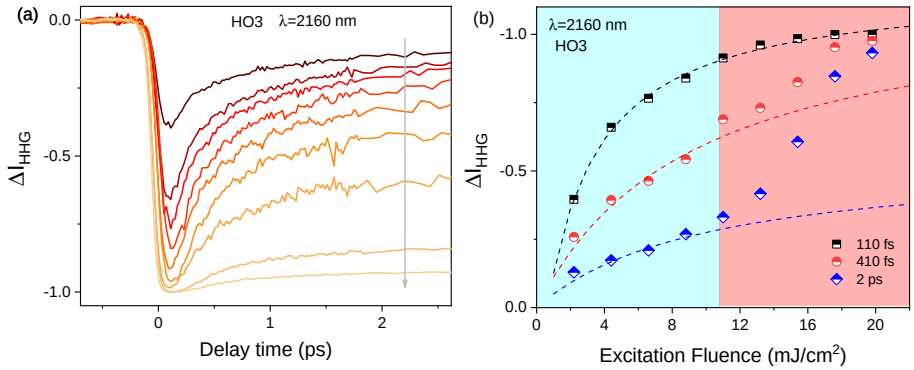

Fig. S6 Transient HHG measurements probed at 2160 nm. (a) Dynamical curves of HO3 and (b) The HHG suppression at three different delay times under different fluences.

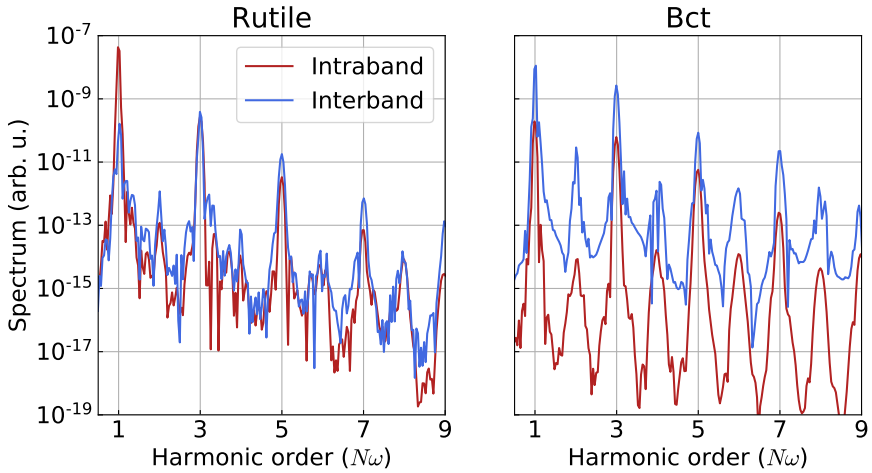

Fig. S7 HHG spectra for both the rutile and *bct* phases where intraband and interband contributions are distinguished clearly.

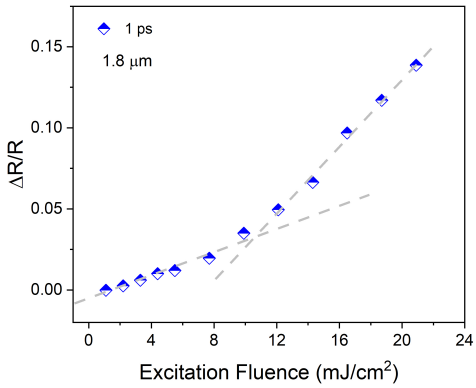

Fig. S8 Transient reflection change of fundamental wavelength (1.8 μm) at 1 ps as a function of the excitation fluence. A slope change can be observed apparently near 11 mJ/cm^2 (the threshold for the phase transition).

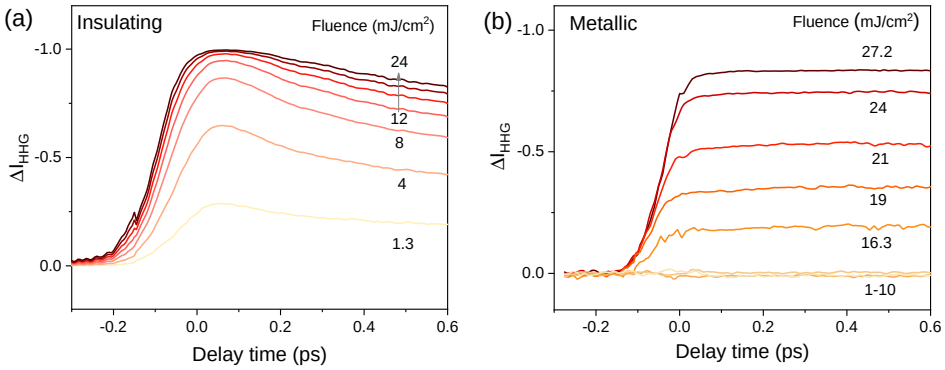

Fig. S9 Transient HHG responses from (a) the semiconducting phase and (b) the metallic phase at a series of excitation fluences, calculated from the saturation model.

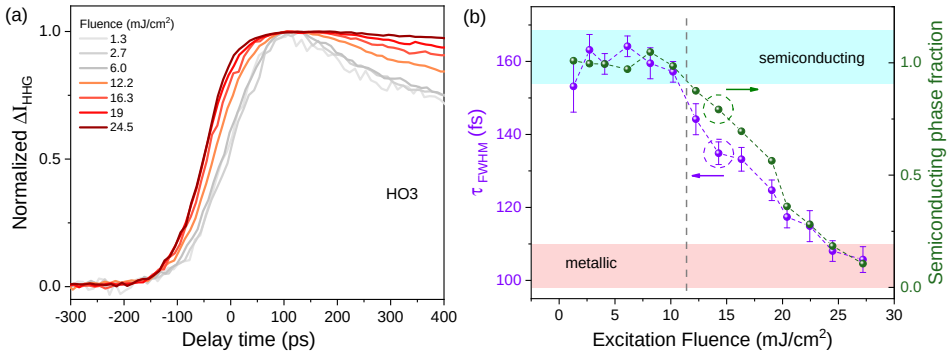

Fig. S10 (a) The normalized dynamical curves of transient signals at HO3, where grey lines are from the low fluence and red lines represent the results above the threshold. (b) The fitted FWHM of the rising edge in (a) as a function of excitation fluences. The semiconducting phase fraction is also plotted for comparison.

II. SUPPLEMENTARY NOTES

A. Material characterizations

The polycrystalline NbO_2 investigated here was grown on a *c*-plane sapphire substrate through reactive bias target ion beam deposition (RBTIBD), and the details of growth conditions can be found elsewhere [1, 2]. The thickness of our sample is determined to be $\sim$ 115 nm by X-ray reflectivity. The Raman spectrum shows two main peaks at 155 and 185 cm^{-1}, consistent with previously reported Raman modes of *bct*-NbO_2 films [3, 4]. In addition, the X-ray diffraction 2θ scan displays only two peaks at $2\theta = 37^{\circ}$ and 79°, corresponding to the (440) and (880) diffractions of *bct*-NbO_2. No Raman or X-ray diffraction peaks of other oxide components (NbO or Nb_2O_5) are observed. Thus, it can be concluded that the studied polycrystalline film is predominantly the semiconducting *bct* phase of NbO_2 with the $(110)_{bct}/(100)_{rutile}$ orientation along the out-of-plane direction.

B. Experimental setup

To measure the static and transient HHG spectra in NbO_2 film, a commercial Ti:Sapphire laser amplification system (Astrella from Coherent) works as the femtosecond laser source, where the 35-fs pulses are generated with a central wavelength of 800 nm. The total pulse energy of 6 mJ is divided into two beams: the majority of laser power for the optical parametric amplification system (OPA) to generate longer wavelengths ranging from 1.6 to 2.4 μm, and the residual part for the frequency doubling to work as the pump beam [5]. The idler pulses of the OPA at 1.8 μm are chosen as a probe and focused onto the sample surface by a f=20cm focusing lens. The pulse duration of the 1.8-μm idler was measured to be 54 fs through FROG and the 400-nm pulse was estimated to be 57 fs via another independent measurement without phase transition. The reflected HHG signals from the sample surface are directly collected by a fiber spectrometer (Avantes). First test measurements were done with and without a lens in front of the fiber, which did not show any difference in measured dynamics. Then, we mounted the fiber entrance on an x-y positioner without the lens, which allowed scanning the fiber over the harmonics over several hundreds of micrometer without changing the signal. This gave us confidence that this was a viable way of collecting the light. Another beam with a frequency doubling to 400 nm works to inject photocarriers into the sample. It should be mentioned that the powers of these two beams can be tuned through waveplates and polarizers, but their polarizations are fixed as *p* polarization for all measurements. To avoid parasitic multiple reflections at the various interfaces for both pump and probe pulses, we applied two larger incident angles for these two beams (60 and 40 degrees for pump and probe). The corresponding spot sizes of 250 and 45 μm for the pump and probe, respectively, ensure homogenous excitation within the probed volume. To measure the transient HHG response, one motorized stage (Physik instruments) is employed to change the optical path of the pump beam, and one optical shutter (Vincent Associates) is also installed in the pump beam to create pump on and off states to extract transient HHG changes.

C. The comparison between perturbative and non-perturbative THG dynamics

As shown in Figure 2(b) and Figure S5(a), the dynamics of HO3 under the perturbative and non-perturbative regimes indeed look quite similar, even though the perturbative response is somewhat less pronounced. In principle, the perturbative HO3 response should also be sensitive to the IMT, because the transition from the insulating to metallic states can alter the material properties a lot and the local nonlinear polarization should be changed during IMT. Due to the difference in the physical origins, the non-perturbative response is theoretically expected to be more sensitive to IMT than the perturbative one.

D. The saturation model for photo-excited HHG

Transient reductions of HHG signals in solids have been reported and investigated in many materials, but the main mechanisms behind the interesting HHG suppression are an open question. According to the microscopic generation process of HHG, the carrier population and dephasing time of coherent electron-hole pairs are supposed to determine signal strengths directly. It has been verified that incoherent carriers have a deleterious influence on these two factors. Such carriers are created by either photoexcitation or electrical doping [6–8]. These incoherent carriers can reduce the tunneling probability of coherent electrons, driven by the probe beam, due to the phase space-filling effect and the variation of the joint density of states between valence and conduction bands. More importantly,

these pre-existing carriers also lead to enhanced electron-electron scattering and largely reduce the dephasing time. Some relevant experiments and simulations reported the scattering enhancement as the main reason for transient HHG change [6, 7, 9]. and photon-echo spectroscopy in GaAs[10] also supports this claim: the dephasing time T_2 of coherent electrons can be phenomenologically described as $T_2 \propto (N+n_0)^{-0.3}$, where n_0 represents the intrinsic carrier density and N defines photocarrier density excited by the pump pulses. Generally, the intrinsic carrier density can be calculated roughly by electrical transport measurements and based on the measured conductivity in our sample at room temperature, n_0 is estimated to be 10^{18} cm^{-3} [1, 11]. although this value is always underestimated and not strictly comparable with photo-excited carriers. Regarding the contribution of pump excitation, the sample absorption and subsequent photocarrier dynamics could help calculate transient carrier density. Our sample shows a nearly constant absorption rate at the investigated fluence range, and the corresponding initial photocarrier density has been mentioned in the main text of this letter. Photocarrier dynamics in NbO_2 have been studied before via transient absorption[2, 12] and the decay equation can be directly used here. Although the microscopic and well-defined mechanism between HHG suppression and the dephasing time is still lacking, the characteristic of transient HHG in semiconductors could be phenomenologically described well by a simple exponential function of the dephasing time T_2: $I_{HHG} \propto e^{-\tau_{HHG}/T_2}$, where τ_{HHG} is one parameter about the emission time of specific harmonic order [6, 7]. Thus transient HHG signals in semiconductors can be linked to the applied excitation fluence. The above model can reproduce well experimental data in Fig. 2 (dash lines) and is named as the saturation model, due to the curve shape. It should be mentioned that the saturation model proposed here is also supported by transient HHG from two-dimensional materials [6, 7, 13] and perovskite thin film recently found but unpublished. The good agreement between experimental data and the saturation model also confirms that HHG changes under low fluence or initial delay times indeed originate from the transient response of the semiconducting phase of NbO_2, so the deviation from the model can be assigned to photo-induced metallization. Moreover, temperature-dependent HHG signals also support the model assumption used above: static HHG signals start dropping with the temperature increase. Higher temperature will lead to higher intrinsic charge density and strengthen electron-electron scattering [1, 11], which both contribute to the reduction of the dephasing time and then suppress HHG emission largely.

In addition, while a previous report on time-resolved high-harmonic spectroscopy in VO_2 has not explicitly shown this steplike change of HHG suppression, our own reanalysis of the author's data from Ref.[14] in fact, shows that the saturation model also fits well transient HHG changes in VO_2 at low fluence and a similar steplike suppression change is likely to present. This implies that fluence dependence studies of time-resolved HHG are a highly sensitive way to probe IMTs.

E. Numerical calculations of high harmonic generation in NbO_2

The field-free band structure and dipole couplings were obtained with the electronic structure code Quantum Espresso [15]. We used a Perdew–Burke-Ernzerhof (PBE) exchange-correlation functional on a Monkhorst–Pack (MP) grid of $9 \times 9 \times 15$ $\boldsymbol{k}$-points for the rutile phase while a MP grid of $4 \times 4 \times 7$ $\boldsymbol{k}$-points was used for the *bct* phase. Afterward, the field-free tight-binding Hamiltonian used for the propagation was constructed by projecting the Bloch bands onto a set of maximally localized Wannier functions using the Wannier90 code [16]. For both phases, the Bloch states were projected onto the d_{z^2}, $d_{x^2-y^2}$, d_{xy}, d_{xz} and d_{yz} orbitals of niobium. For the *bct* phase, this meant a total number of 160 orbitals, while for the rutile phase, it meant only 10 orbitals.

The response of the material to the laser field was then obtained by numerically solving the semiconductor Bloch equations in the Wannier gauge, as described in ref. [17]. We simulated the interaction of both phases with a probe field with matching parameters of those used in the experiments: a linearly-polarized 1.8 μm field with an intensity of 0.2 TW/cm^2. While the theoretical intensity of the laser field does not completely match the experimental one, we have ensured that we are in the non-perturbative regime, so we can accurately and safely compare the experimental results with the theoretical ones. The excitation should occur at the point where the bandgap is, i.e. at the Γ-point. Since both phases have quite different unit cells, the directions of the laser field should also be different. We choose that specific direction, precisely the x-direction in the *bct* phase and inclined 45 degrees with respect to the x and y directions for the rutile phase, because it is where all the Nb-O bonds lie and therefore, where all the dynamics will happen. In momentum space, the situation gets a bit more complicated. As shown in Fig. 3(a) of the band structure of the material, there is a huge overlap between different bands. This means that the charge carriers will be able to move in almost all symmetry directions (in k-space). To accurately compare both spectra, we first projected the currents in the same direction. For the *bct* simulation, we used a MP grid of $20 \times 8 \times 2$ $\boldsymbol{k}$-points while for the rutile's case, we used a MP grid of $100 \times 100 \times 8$ $\boldsymbol{k}$-points. We checked that the results were properly converged for both cases. The calculated HHG spectra from both phases have been displayed in Figures 3 and S7. Our simulations also separate the intraband and interband contributions in both phases shown in Figure S7 and support that interband polarization might play a significant role in our observed HHG spectra. In a system such as NbO_2, where one has hundreds of

bands, it is rather complicated to completely ensure that the origin of the current is either intraband or interband. Indeed, the more likely scenario is that the origin is a complex combination of the two mechanisms. It is also likely that even higher harmonics would be dominated stronger by the interband mechanisms, however the defect emission and damage threshold of our polycrystalline sample make those higher harmonics, or even a plateau-like emission as could be expected for the interband mechanism, difficult to observe in the current experiments. Future studies that may aim to shed more light on the HHG mechanism should address this by using single-crystalline samples and shorter infrared driving pulses.

Alongside the full *ab-initio* calculation, we also developed a simplified model, to gain more physical insight, based on the Peierls model for one-dimensional dislocations. It consists of a one-dimensional chain with two atoms per unit cell with two types of hoppings, intracell (between atoms inside the same unit cell) and intercell (between different unit cells). The Hamiltonian for such a chain is simply:

$$H = \sum_x t_{\text{intra}} b_x^\dagger a_x + t_{\text{inter}} a_{x+1}^\dagger b_x + \text{h.c.}, \tag{1}$$

where $c_x/c_x^\dagger$ is the creation/annihilation operator on site x with c being either a or b. This model has two different phases depending on the magnitude of the hopping parameters. If $t_{\text{intra}} > t_{\text{inter}}$ the system will be insulating with a gap of magnitude $\Delta \sim |t_{\text{intra}} - t_{\text{inter}}|$. However, when both hopping parameters are equal ($t_{\text{intra}} = t_{\text{inter}}$), the system will be metallic as the gap vanishes. Such an atomic chain is also known as the Su–Schrieffer–Heeger (SSH) model. We are aware that this system can host topological phases [18]. However, those states only appears when we have a finite chain, and since we are working with a system with periodic boundary condition, there are no differences between the trivial and the "topological" regimes.

To mimic what happens in NbO_2, we will parameterise the hopping parameters as

$$t_{\text{intra/inter}} = t_0 \exp\left(-\frac{d_T/2 - d_{\text{intra/inter}}}{d_T}\right) \tag{2}$$

where $d_T = d_{\text{intra}} + d_{\text{inter}} = 3.5$ Å, which is similar to the Nb-O bond distance in the *bct* phase, and $t_0 = 1$ eV. We selected those parameters so to match the physics of NbO_2. Using this parametrization, this atomic chain will be only metallic when $d_{\text{intra}} = d_{\text{inter}}$. Therefore, by tuning the bonding distances, we will move between insulating and metallic states. The laser parameters were the same as in the *ab-initio* calculation and also the dynamics were solved using the same scheme. We used a grid of 500 $\boldsymbol{k}$-points for the simulations.

F. The timescale extraction of transient metallization

Experimental and theoretical studies both confirm that the excitation fluence beyond F_{th} can trigger transient metallization in NbO_2, and the efficiency difference of semiconducting and metallic phases leads to HHG deviation from the saturation model. Interestingly, such deviation increases gradually rather than suddenly. According to previous research on phase transition, this fluence-dependent feature can be explained by the second-order transition or the spatial inhomogeneity of phase transition. Coherent phonon spectroscopy in NbO_2 shows no obvious phonon softening and the former hypothesis (second-order transition) can be safely ruled out [2]. Spatial inhomogeneity of IMT has been found in correlated materials, including VO_2, via ultrafast microscopy and nano-imaging techniques, and generally assigned to crystal imperfections. The local crystal changes, such as element doping or lattice defects, can result in the entropy increase, and accordingly, reduce the enthalpy requirement for phase transition. Hence, this spatial inhomogeneity could be enabled by the polycrystalline nature of our sample, and local information of IMT, such as the metallic phase fraction P, can be derived from transient HHG changes. It can be assumed that both the newly formed metallic and residual semiconducting phases simultaneously contribute to HHG emission, and considering the much weaker efficiency of the metallic phase, transient HHG signals can be approximately written as:

$$I_{HHG} = P * \alpha_{metal} + (1 - P) * \alpha_s(N, t) \tag{3}$$

where I_{HHG} is the detected HHG signal, and α_{metal} and $\alpha_s(N, t)$ are HHG efficiency of the metallic and semiconducting phases respectively. It should be noted that α_{metal} can be found from the above simulation and immune to carrier dynamics after metallization, and $\alpha_s(N, t)$ can be calculated by the proposed saturation model related to the excitation fluence and delay time. Via applying Equation (3) to fit experimental data after IMT, e.g. 0.3 and 1 ps in Fig. 2, phase fraction P at different delay times can be extracted and plotted in Fig. 4(a). The phase fraction strongly relies on the excitation fluence and starts increasing beyond F_{th}. A uniform phase transition can be achieved in our sample when the excitation fluence approaches the damage threshold. This phase diagram reveals that transient metallization in NbO_2 is a nanoscale nucleation process related to the excitation fluence.

Except for the phase diagram, the timescale of IMT can be also extracted from transient HHG changes in Fig. 2 by using Equation (3). The proposed saturation model manages to reproduce the HHG response of the semiconducting phase to the excitation fluence and delay time, as shown in Fig. S9(a). Combined with the metallic phase fraction P, the isolated IMT response (i.e. the metallic response $P * \alpha_{metal}$) can be calculated and plotted in Fig. S9(b) at a serial of excitation fluences. At low fluence transient HHG changes from the metallic phase are almost negligible. Beyond the threshold F_{th}, HHG signals exhibit a sudden change (reduction), meaning the emergence of the metallic phase. The amplitude of HHG changes in Fig. S9(b) originates from the metallic phase fraction, consistent with Fig. 4(a). As the derivative operation increases noise on experimental data, we chose another (equivalent) method based on the error function to fit the HHG change shown in the inset of Fig. 4(b). The equation can be written as:

$$\Delta I_{HHG} = [1 + erf(\frac{t-b}{\tau_p})][A_1 e^{-t/\tau_1} + A_2 e^{-t/\tau_2} + c] \tag{4}$$

where b and τ_p are the offset and width of the error function to describe the rising edge and the second brocket represents the subsequent decay processes. According to the mathematical definition of the error function,the full width at half maximum (FWHM) of the rising edge should be equal to $\sqrt{4ln2}\tau_p$. The emergence rate of HHG suppression corresponds to the IMT timescale, and its fitted FWHM values are plotted as a function of the excitation fluence in Fig. 4(b). Considering the uncertainty of measurements and the fitting errors, the FWHM of the IMT timescale stays nearly constant (90-110 fs) for the applied excitation fluences. To verify this analysis, we also normalized experimental data for all excitation fluences and directly fit those rising edges, which are summarized and shown in Fig. S10. The FWHM of the rising edge seems to be constant below F_{th}, and then starts decreasing with the fluence increase until the damage threshold. Such interesting dependence of the rising edge is nearly in accordance with the fraction change of the metallic phase. Thus, the constant FWHM ($\sim$ 160 fs) of the rising edge at low fluence represents the intrinsic HHG response of the semiconducting phase, and the smallest FWHM ($\sim$ 105 fs) means the timescale of IMT or metallization. The intermediate regime is a mixture of two phases, and the rising time is affected by two different responses. Shorter pulses and better models or simulations will help distinguish the nature of IMT.

G. The estimation of lattice temperature

Based on the assumption that all absorbed laser energy can be dissipated through lattice heating without any other significant consumption, the lattice temperature rise induced by laser excitation can be estimated by the equation below:

$$\alpha F_{pump} = \frac{t\beta}{M} \int C_p dT \tag{5}$$

where the left side represents the total energy absorbed by NbO_2, and the right side corresponds to the required energy for a certain temperature rise. Thus, α is the absorption of the pump pulses which is measured to be 0.6 for the sample in this study, and F_{Pump} is the pump fluence. And t is the sample thickness here. M and β are the molar mass and density of NbO_2, which are 124.9 g/mol, and 5.9 g/cm^3 respectively. C_p is the heat capacity of NbO_2, as a function of the lattice temperature. Using the equation and parameters above, the relationship between the excitation fluence and the estimated maximum lattice temperature can be calculated. The fluence threshold found in HHG measurements (12-13 mJ/cm^2) can only heat the sample to nearly 500K - this number represents an upper limit in the present conditions as elaborated above - which is still not sufficient to trigger IMT thermally (>1000 K). Moreover, considering the phonon emission time and phono-phonon interaction, energy transfer to heat lattice cannot occur within the timescale of IMT extracted from HHG. It can be safely concluded that the transition occurring at the fluence threshold is a non-thermal one and generally transient influence from photo-excited carriers on atomic bonding or lattice distortion should be the main driver for the non-thermal phase transition, which deserves further investigation.

[1] Y. Wang, R. B. Comes, S. Kittiwatanakul, S. A. Wolf, and J. Lu, Epitaxial niobium dioxide thin films by reactive-biased target ion beam deposition, Journal of Vacuum Science & Technology A: Vacuum, Surfaces, and Films **33**, 021516 (2015).

[2] Y. Wang, Z. Nie, Y. Shi, Y. Wang, and F. Wang, Coherent vibrational dynamics of NbO_2 film, Physical Review Materials **6**, 035005 (2022).

[3] K. Shibuya and A. Sawa, Epitaxial growth and polarized raman scattering of niobium dioxide films, AIP Advances **12**, 055103 (2022).

[4] G. J. Páez Fajardo, S. A. Howard, E. Evlyukhin, M. J. Wahila, W. R. Mondal, M. Zuba, J. E. Boschker, H. Paik, D. G. Schlom, J. T. Sadowski, *et al.*, Structural phase transitions of NbO_2: bulk versus surface, Chemistry of Materials **33**, 1416 (2021).

[5] G. de Haan, T. van Den Hooven, and P. Planken, Ultrafast laser-induced strain waves in thin ruthenium layers, Optics Express **29**, 32051 (2021).

[6] C. Heide, Y. Kobayashi, A. C. Johnson, F. Liu, T. F. Heinz, D. A. Reis, and S. Ghimire, Probing electron-hole coherence in strongly driven 2d materials using high-harmonic generation, Optica **9**, 512 (2022).

[7] K. Nagai, K. Uchida, S. Kusaba, T. Endo, Y. Miyata, and K. Tanaka, Effect of incoherent electron-hole pairs on high harmonic generation in atomically thin semiconductors, arXiv preprint arXiv:2112.12951 (2021).

[8] H. Nishidome, K. Nagai, K. Uchida, Y. Ichinose, Y. Yomogida, Y. Miyata, K. Tanaka, and K. Yanagi, Control of high-harmonic generation by tuning the electronic structure and carrier injection, Nano Letters **20**, 6215 (2020).

[9] G. G. Brown, Á. Jiménez-Galán, R. E. Silva, and M. Ivanov, A real-space perspective on dephasing in solid-state high harmonic generation, arXiv preprint arXiv:2210.16889 (2022).

[10] P. Becker, H. Fragnito, C. B. Cruz, R. Fork, J. Cunningham, J. Henry, and C. Shank, Femtosecond photon echoes from band-to-band transitions in gaas, Physical Review Letters **61**, 1647 (1988).

[11] Y. Sakai, N. Tsuda, and T. Sakata, Electrical properties of semiconducting NbO_2, Journal of the Physical Society of Japan **54**, 1514 (1985).

[12] J. K. Clark, Y.-L. Ho, H. Matsui, H. Tabata, and J.-J. Delaunay, Thresholdless behavior and linearity of the optically induced metallization of NbO_2, Physical Review Research **1**, 033168 (2019).

[13] Y. Cheng, H. Hong, H. Zhao, C. Wu, Y. Pan, C. Liu, Y. Zuo, Z. Zhang, J. Xie, J. Wang, *et al.*, Ultrafast optical modulation of harmonic generation in two-dimensional materials, Nano Letters **20**, 8053 (2020).

[14] M. R. Bionta, E. Haddad, A. Leblanc, V. Gruson, P. Lassonde, H. Ibrahim, J. Chaillou, N. Émond, M. R. Otto, Á. Jiménez-Galán, *et al.*, Tracking ultrafast solid-state dynamics using high harmonic spectroscopy, Physical Review Research **3**, 023250 (2021).

[15] P. Giannozzi, S. Baroni, N. Bonini, M. Calandra, R. Car, C. Cavazzoni, D. Ceresoli, G. L. Chiarotti, M. Cococcioni, I. Dabo, A. D. Corso, S. de Gironcoli, S. Fabris, G. Fratesi, R. Gebauer, U. Gerstmann, C. Gougoussis, A. Kokalj, M. Lazzeri, L. Martin-Samos, N. Marzari, F. Mauri, R. Mazzarello, S. Paolini, A. Pasquarello, L. Paulatto, C. Sbraccia, S. Scandolo, G. Sclauzero, A. P. Seitsonen, A. Smogunov, P. Umari, and R. M. Wentzcovitch, Quantum espresso: a modular and open-source software project for quantum simulations of materials, Journal of Physics: Condensed Matter **21**, 395502 (2009).

[16] A. A. Mostofi, J. R. Yates, G. Pizzi, Y.-S. Lee, I. Souza, D. Vanderbilt, and N. Marzari, An updated version of wannier90: A tool for obtaining maximally-localised wannier functions, Computer Physics Communications **185**, 2309 (2014).

[17] R. E. F. Silva, F. Martín, and M. Ivanov, High harmonic generation in crystals using maximally localized wannier functions, Phys. Rev. B **100**, 195201 (2019).

[18] D. Vanderbilt, *Berry Phases in Electronic Structure Theory* (Cambridge University Press, 2018).